



Delft University of Technology

General Analytical Modeling for Magnet Demagnetization in Surface Mounted Permanent Magnet Machines

Guo, Baocheng; Huang, Yunkai; Peng, Fei; Dong, Jianning

DOI

[10.1109/TIE.2018.2873099](https://doi.org/10.1109/TIE.2018.2873099)

Publication date

2019

Document Version

Final published version

Published in

IEEE Transactions on Industrial Electronics

Citation (APA)

Guo, B., Huang, Y., Peng, F., & Dong, J. (2019). General Analytical Modeling for Magnet Demagnetization in Surface Mounted Permanent Magnet Machines. *IEEE Transactions on Industrial Electronics*, 66(8), 5830-5838. Article 8482461. <https://doi.org/10.1109/TIE.2018.2873099>

Important note

To cite this publication, please use the final published version (if applicable).

Please check the document version above.

Copyright

Other than for strictly personal use, it is not permitted to download, forward or distribute the text or part of it, without the consent of the author(s) and/or copyright holder(s), unless the work is under an open content license such as Creative Commons.

Takedown policy

Please contact us and provide details if you believe this document breaches copyrights.

We will remove access to the work immediately and investigate your claim.

Green Open Access added to TU Delft Institutional Repository

'You share, we take care!' - Taverne project

<https://www.openaccess.nl/en/you-share-we-take-care>

Otherwise as indicated in the copyright section: the publisher is the copyright holder of this work and the author uses the Dutch legislation to make this work public.

General Analytical Modeling for Magnet Demagnetization in Surface Mounted Permanent Magnet Machines

Baocheng Guo , Member, IEEE, Yunkai Huang , Fei Peng, Member, IEEE, and Jianning Dong , Member, IEEE

Abstract—This paper proposes an analytical model for the prediction of airgap magnetic field distribution for axial flux permanent magnet (AFPM) machine with partial magnet demagnetization. The AFPM machine geometry is first converted to a polar representation. Consequently, the subdomain model based on current sheet technique is developed. Then current sheet representation of PM is derived to consider the partial demagnetization using superposition principle. The back electromagnetic forces and cogging torque are obtained accordingly based on Maxwell's equations. The results show that the results of proposed approach agrees with that of finite-element method. The model is further validated by experiments under both healthy and demagnetized conditions, which can validate the proposed approach. Main contribution of the work is to consider the partial irreversible demagnetization. Moreover, the proposed method is applicable for both AFPM and radial flux permanent magnet machine.

Index Terms—Axial flux permanent magnet (AFPM) machine, current sheet model, demagnetization, magnetic field.

I. INTRODUCTION

A XIAL flux permanent magnet (AFPM) machines, due to their compact mechanical structure and high power density, are promising in many industrial applications, such as the electric vehicles [1], [2], wind power generation [3], and flywheel energy storage system [4], [5]. Just like radial flux permanent magnet (RFPM) electrical machines, AFPM machines suffer from magnet demagnetization since the permanent mag-

Manuscript received May 2, 2018; revised July 24, 2018 and September 4, 2018; accepted September 6, 2018. Date of publication October 5, 2018; date of current version March 29, 2019. This work was supported in part by the National Nature Science Foundation of China under Grant 51777034, in part by the State Key Laboratory of Reliability and Intelligence of Electrical Equipment of Hebei University of Technology under Grant EERIKF2018009, in part by the Qing Lan Project. (Corresponding author: Baocheng Guo.)

B. Guo, Y. Huang, and F. Peng are with the School of Electrical Engineering, Southeast University, Nanjing 210096, China (e-mail: guobaocheng1986@gmail.com; huangyk@seu.edu.cn; pengfei@seu.edu.cn).

J. Dong is with the Department of Electrical Sustainable Energy, Delft University of Technology, 2628CD Delft, The Netherlands (e-mail: J.Dong-4@tudelft.nl).

Color versions of one or more of the figures in this paper are available online at <http://ieeexplore.ieee.org>.

Digital Object Identifier 10.1109/TIE.2018.2873099

net (PM) is sensitive to high temperature, which may cause partial or even complete irreversible demagnetization. Although PM demagnetization may occur only 6%, as shown in [6], it is more vulnerable for PM machines because the loss of magnetization may lead to disordered magnetic field distribution (MFD), and hence causing serious problems, for instance, the unbalance magnetic force and mechanical vibration [7], which could affect normal operation and safety. Therefore, the defects should be analyzed and detected quickly to avoid further damages.

A significant amount of work has been done concerning the demagnetization of PM machines. At present, the numerical approach, such as finite-element method (FEM), is widely used in demagnetization simulation since it is regarded as the most accurate method. For example, Zhu studied the performance of flux switching machine under irreversible demagnetization using FEM [8], while Gilsu studied the demagnetization in various types of electrical machines in [9]. However, it is time consuming. An alternative method to reduce the computation time is the field reconstruction (FR) method proposed in [10], which is partly based on the FEM model. In [10], the author adopted the FR approach to study the electromagnetic vibrations. Although it is much faster than three-dimensional/two-dimensional (3-D/2-D) FE models, it still requires considerable computation time. Moreover, the partial magnet demagnetization of AFPM needs a number of computational layers which takes more time [11].

Analytical or semianalytical approaches, due to their fast and acceptable accuracy, are regarded as efficient and favorable methods. Although the magnetic equivalent circuit (MEC) method [12], [13] can improve computation efficiency, it is complicated to build up the MEC model for the whole machine when the PM has partial demagnetization. Moreover, the accuracy of some qualities like cogging torque and forces are largely affected by the number of nodes and the calculation strategy.

Alternative analytical approaches are mostly Fourier series based methods. They use the solution of Poisson's and Laplace's equations. In the literature [14] and [15], the magnetization vector is adopted. Zhou *et al.* [16] proposed another approach based on the equivalent current sheet representation of single magnet, moreover, this technique simplifies the two subdomains, viz., permanent magnet and air gap, into one. Thereby, the dimension of unknown coefficient matrix is deduced. In [17] and [18], the airgap MFD of a YASA (yokeless and segmented

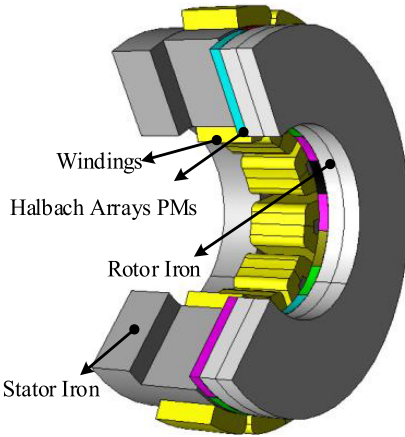


Fig. 1. Configuration of the AFPM machine.

armature) type is calculated by introducing magnetization factor to consider the whole permanent magnet demagnetization, which limits the application of the method. Most, if not all, previous studies do not provide simple and general solutions for partial demagnetization of surface mounted PM machines, including RFPM machine.

To overcome aforementioned problems, this paper proposes an analytical model based on current sheet approach to predict the performance under partial magnet demagnetization. The scaling technique is introduced to avoid ill-conditioned matrix. Compared to previous studies, the proposed method is effective to both AFPM and RFPM machines. It can consider magnetization in any directions, which means it can be used to analyze machines with Halbach arrays.

This paper is organized as follows. In Section II, the parameters of prototype are provided. Section III introduces the equivalent between AFPM and RFPM. The subdomain (SD) model based on current sheet technique is presented in Section IV. Afterward, the results are then discussed in Section V. In Section VI, the experiment results are presented and compared with the results obtained from the proposed approach. Conclusions are drawn at the end of the paper.

II. DESCRIPTION OF PROTOTYPE

In this paper, a 10-slot/4-pole five-phase AFPM machine with concentrated coils is introduced to verify the proposed method, as shown in Fig. 1. The amorphous magnetic material (AMM) is adopted to reduce the iron loss. However, this machine has to be designed with an open slot topology because of limited cutting techniques available and material properties of AMM [19]. Thanks to the Halbach array, flux density in the airgap can be improved to the acceptable level even with open slots. The basic dimensions of prototype are listed in Table I.

III. MODEL OF AFPM

A quasi-3-D-method is used to convert a 3-D model to a 2-D model to reduce the computation time. The machine is divided into a number of layers with a cylindrical cross section.

TABLE I
MAIN DIMENSIONS AND PARAMETERS OF THE STUDIED MACHINE

Symbol	AFPM Quantity	Value and unit
P	Rated power	10 kW
n_{sp}	Rated speed	15,000 rpm
p/Q	Number of pole pairs/slots	2/10
R_o^a/R_i^a	Outer/inner radius of AFPM	100/50 mm
g	Length of air gap	3 mm
B_r	Remanence of magnet	0.75 T
	Magnet Type	Bonded

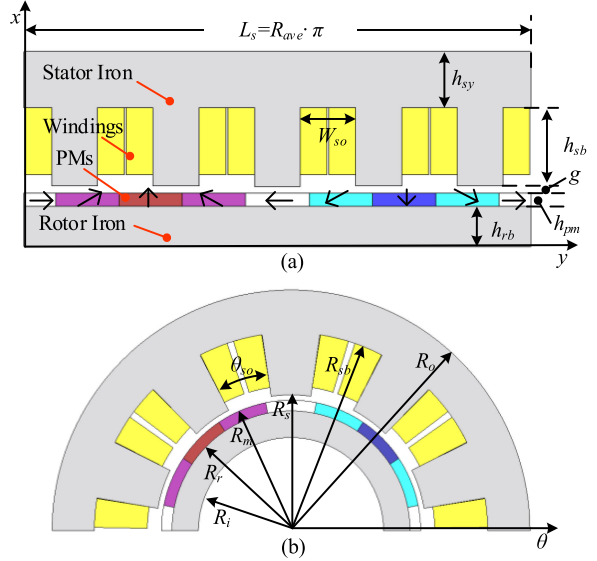


Fig. 2. Analytical model for AFPM machine. (a) Analytical model in Cartesian coordinates. (b) Converted model in polar coordinates.

Afterward, the AFPM can be considered to be composed of several 2-D calculation planes, as shown in Fig. 2(a). In order to simulate partial magnet demagnetization at different location and obtain more accurate results, five slices are chosen in this paper. The average radius R_{ave} of the k th layer is given by

$$R_{ave}^k = R_i^a + \frac{R_o^a - R_i^a}{2n_{sl}}(2k - 1), \quad k = 1, 2, \dots, n \quad (1)$$

$$t_{cp} = \frac{R_o^a - R_i^a}{n_{sl}} \quad (2)$$

where n_{sl} is the number of the slices, and t_{cp} is the width of the slices.

Fig. 2(a) illustrates one layer of the 2-D analytical model of AFPM in the Cartesian coordinate system. The parameters of the AFPM are: L_s is the length of computational domain, h_{rb} is the height of the back-iron, h_{pm} is the height of the PMs, h_{sb} is the depth of slots, h_{sy} stands for the height of stator back iron, and w_{so} stands for the slot opening width. In order to propose a general analytical solution, the equivalent analytical technique to approximate the AFPM as a RFPM presented in [20] is adopted. Fig. 2(b) shows the equivalent RFPM. It should be noted that the air-gap length are sensitive parameters; therefore, the equivalent mean air gap radius R_{ave} is kept un-

TABLE II
RELATIONSHIPS BETWEEN TWO COORDINATES

Symbol	RFPM Quantity	Equivalent Value
R_s	Stator inner radius	$R_{ave} + g/2$
R_{sb}	Stator yoke radius	$R_s + h_{sb}$
R_o	Stator outer radius	$R_{sb} + h_{sy}$
R_m	Radius of PMs	$R_{ave} - g/2$
R_r	Rotor outer radius	$R_m - h_{pm}$
R_i	Rotor inner radius	$R_r - h_{rb}$
θ_{so}	Slot opening	W_{so}/R_{ave}
L	Equivalent stack length	t_{cp}

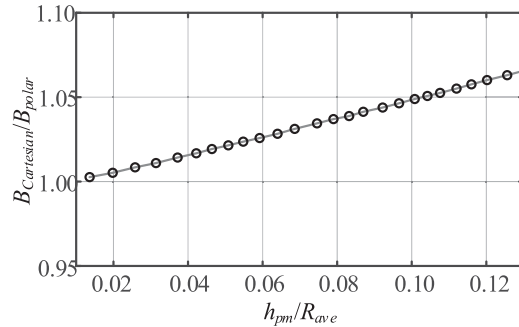


Fig. 3. Ratio between the two coordinates.

changed in the equivalent. The relationship between the dimensions of the equivalent RFPM and the AFPM are listed in Table II.

Therefore, the analytical model of AFPM in Cartesian coordinate system is converted to a polar coordinate system, as shown in the above equivalent approximation. The proposed model in this paper can be used in both AFPM and RFPM machines.

The equivalent analytical model needs a correction factor to calibrate the final results. The parameter of importance is the value of the ratio between the magnet radial thickness and the mean airgap radius. The slotless analytical models developed in Cartesian [21] and polar [22] coordinates are adopted to calculate the correction coefficient. By varying the magnet thickness of investigated AFPM machine between 0.001 m and 0.01 m, the ratio between the no-load flux obtained from the two coordinates is shown in Fig. 3. It can be seen that the difference is less than 7%. By applying the correction factor to the final flux density results, higher accuracy can be achieved.

IV. ANALYTICAL SOLUTION OF MAGNETIC FIELD

The subdomain model is chosen to calculate the magnetic field. Normally, several assumptions are made to simplify the calculation: 1) the iron materials have infinite permeability; 2) the end effect and eddy current effect are ignored; and 3) the magnetic material has uniform magnetization, and the relative recoil permeability μ_r is constant.

A. Equivalent Surface Current of Magnet

The current sheet technique based on [16] is improved in this paper. The scaling technique and magnetization direction are considered for the sake of the general solutions. The calculation

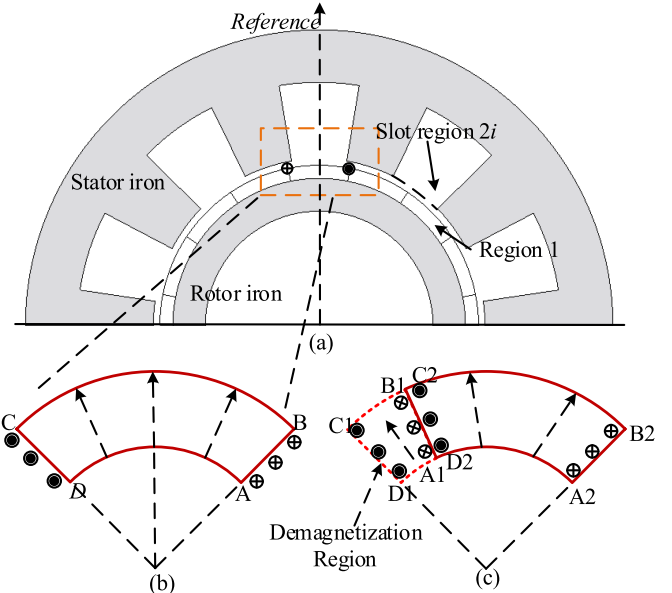


Fig. 4. Subdomain model. (a) Computed region. (b) Current sheet distribution under normal condition. (c) Current sheet distribution under partial demagnetization.

model can be seen in Fig. 4(a). Afterward, the exact SD model can be separated into two domains, as shown in Fig. 4(a), viz., air gap and PM region (region 1) and slot region (2i).

The magnetization of PM in AFPM is in parallel since the PMs are flat, however, after converting it into the polar system, the magnetization is also changed. The magnetization direction is changed to radial, as shown in Fig. 4(b).

The magnetization vector M can be replaced by a pair of magnetizing currents, which means that the single PM can be modeled by sheet current. This feature is very suitable for modeling partial demagnetization, as shown in Fig. 4(c), which means the current sheet can be separated into two parts and calculated separately, afterward, the superposition principle can be applied.

The magnetization vector is given by

$$\vec{M} = M_r \vec{e}_r + M_\theta \vec{e}_\theta \quad (3)$$

where M_r and M_θ are the radial and tangential components, respectively. e_r and e_θ are radial and tangential unit, respectively.

For radial magnetization, the linear current density of sides AB and CD can be presented as

$$J = H_{cj} \quad (4)$$

where H_{cj} is the coercivity of PM.

It should be noted that the AFPM machine investigated in this paper has Halbach arrays, four-segment array is chosen in this machine and the PMs can be defined as end, side and middle PM, as shown in Fig. 5. Different magnetization can be replaced by combining radial and circumferential magnetization.

After replacing M by virtual equivalent surface current J , the radial J_r and circumferential direction J_θ of equivalent surface current are given by

$$J_r = J \cdot \sin(\theta_{pm}), J_\theta = J \cdot \cos(\theta_{pm}) \quad (5)$$

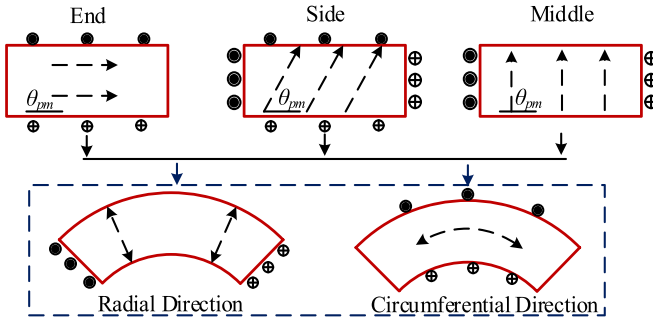


Fig. 5. PM under different magnetization.

where θ_{pm} is the magnetization direction.

Subsequently, the PMs are divided into a number of current sheets at radius r with a linear current. The total current of the equivalent coil can be expressed as

$$i_c = J_x \Delta l \quad (6)$$

where J_x is the radial and circumferential current density shown in (5). Δl is the length infinitesimal in the sides AB, CD, AD, and BC of the magnet pole.

B. Magnetic Field Calculation

Both region 1 (PM and airgap) and region 2i (Slot) satisfy the Laplace equation. For the 2-D case in the polar coordinate system, by introducing magnetic vector potential A , the governing function is

$$\frac{\partial^2 A}{\partial r^2} + \frac{1}{r} \frac{\partial A}{\partial r} + \frac{1}{r^2} \frac{\partial^2 A}{\partial \theta^2} = 0. \quad (7)$$

The solution of Laplace equation can be obtained using separation of variables. Taking into account the boundary condition, the general solution of vector potential A in region 1 can be obtained. In order to avoid ill-conditioned matrix, the scaling technique is introduced as

$$P_\omega(u, v) = \left(\frac{u}{v}\right)^\omega + \left(\frac{v}{u}\right)^\omega, E_\omega(u, v) = \left(\frac{u}{v}\right)^\omega - \left(\frac{v}{u}\right)^\omega \quad (8)$$

where u , v , and w are the system variables.

Afterward, the general solution of vector potential A in region 1 of j th permanent magnet is simplified as

$$A_I(r, \theta) = (-1)^{j-1} \left\{ \sum_{m=1}^{\infty} \left(A_m^I \frac{P_m(r, R_r)}{P_m(R_s, R_r)} + X_\theta \right) \cos(m\theta) + \sum_{m=1}^{\infty} \left(C_m^I \frac{P_m(r, R_r)}{P_m(R_s, R_r)} + X_r \right) \sin(m\theta) \right\} \quad (9)$$

where

$$X_r = \frac{\mu_0 i_c}{m\pi} \frac{R_r^{2m} + a^{2m}}{a^m} r^{-m} \sin(m\varphi) \quad (10)$$

$$X_\theta = r \frac{\mu_0 i_c}{\pi} \frac{R_r^{2m} + a^{2m}}{a^m} r^{-m} \sin(m\varphi) \quad (11)$$

where a is the radius of current sheet.

The angular position of the i th stator slot is defined as

$$\theta_i = -\frac{\theta_{so}}{2} + \frac{2i\pi}{Q}, 1 \leq i \leq Q. \quad (12)$$

The general solution of region $2i$ is

$$A_{2i} = A_0^{2i} + B_0^{2i} \ln r + \sum_{k=1}^{\infty} \left(A_k^{2i} \frac{P_{k\pi/\beta}(r, R_{so})}{P_{k\pi/\beta}(R_s, R_{so})} \right) \cdot \cos \left(\frac{k\pi}{\theta_{so}} (\theta - \theta_i) \right) \quad (13)$$

where A_m^I , C_m^I , A_0^{2i} , B_0^{2i} , and A_k^{2i} , are coefficients to be determined. m and k are harmonic order in each computed domain.

An additional constraint between the coefficients B_0^{2i} apply to (13)

$$\sum_{i=1}^Q B_0^{2i} = 0. \quad (14)$$

It should be noted that each domain is connected, so the interface conditions should meet. The one between region 1 and region i at R_s is

$$A_1(R, \theta) = A_{2i}(R, \theta), \theta_i - \frac{\theta_{so}}{2} \leq \theta \leq \theta_i + \frac{\theta_{so}}{2} \quad (15)$$

$$\begin{cases} H_{x1}(R, \theta) = H_{x2i}(R, \theta), & \theta_i - \frac{\theta_{so}}{2} \leq \theta \leq \theta_i + \frac{\theta_{so}}{2} \\ H_{x1}(R, \theta) = 0, & \text{elsewhere} \end{cases}. \quad (16)$$

The unknown coefficients can be obtained by applying Fourier series expansion and boundary conditions. The final equations are shown in the following:

$$\begin{bmatrix} K_{11} & 0 & K_{13} & 0 \\ 0 & K_{22} & K_{23} & 0 \\ K_{31} & K_{32} & K_{33} & 0 \\ K_{41} & K_{42} & 0 & K_{44} \end{bmatrix} \begin{bmatrix} A_m^1 \\ C_m^1 \\ A_k^i \\ A_0^i \end{bmatrix} = \begin{bmatrix} I_1 \\ I_2 \\ I_3 \\ I_4 \end{bmatrix} \quad (17)$$

where $K_{11}-K_{14}$ and I_1-I_4 are the coefficients obtained by the solution strategy in [16].

The superposition principle can be applied to the vector potential, for example, the equivalent surface current of sides AB and CD can be obtained.

Afterward, the radial and tangential flux density components are obtained

$$B_r = \frac{1}{r} \frac{\partial A}{\partial \theta}, B_t = -\frac{\partial A}{\partial r}. \quad (18)$$

Hence, the on-load flux densities could be obtained by superposition of each PM.

V. RESULTS AND ANALYSIS

A. Normal Performance

The proposed method is verified by 3-D nonlinear FEM model, as shown in Fig. 6. It should be noted that, the magnetization direction θ_{pm} of middle, side, and end PM are 90° , 35° , and 0° , respectively.

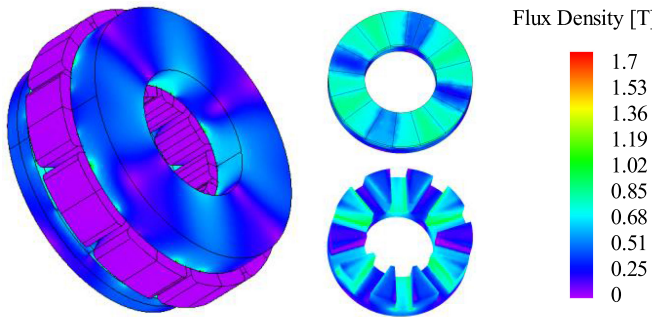


Fig. 6. FE model of the AFPM.

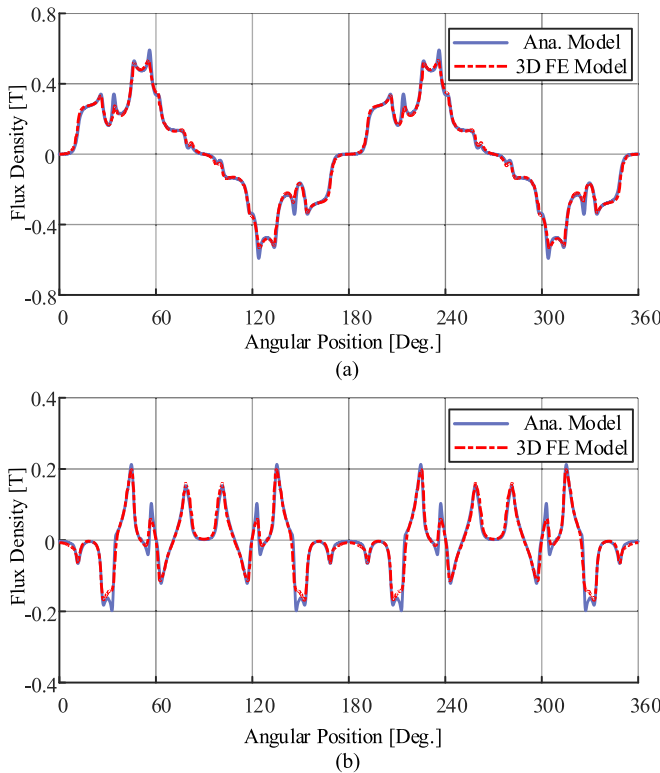


Fig. 7. No-load airgap flux density waveforms of proposed method and FEM under normal condition. (a) Radial component. (b) Tangential component.

Fig. 7 compares the flux density in the middle circle of the airgap. It shows that the results predicted by the proposed method agree well with those obtained from the FEM model.

Under no-load condition, the flux over each slot (φ_j) is

$$\varphi_j = N_c \cdot \int_{\theta_0}^{\theta_0 + \theta_c} F_{Dc,s} B_r(R_a, \theta) d\theta \quad (19)$$

where N_c is the number of turns in series per phase, θ_0 is the coil starting side angle from the origin, θ_c is the expansion angle of the coil pitch, and F_{Dc} is coil distribution function as shown

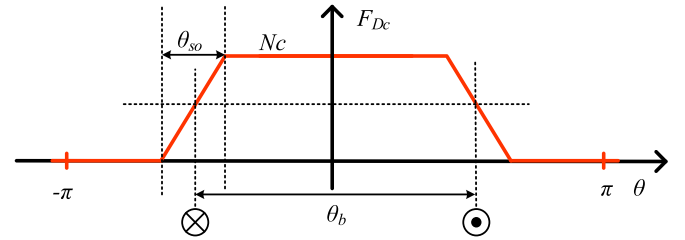


Fig. 8. Distribution function of coil.

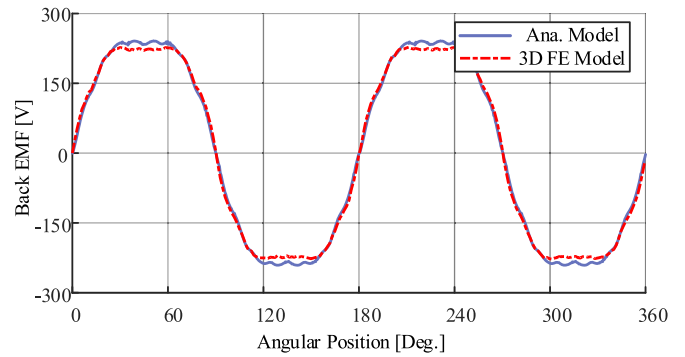


Fig. 9. Back-EMF under normal condition.

in Fig. 8 and it can be expressed as [23]:

$$F_{Dc}(\theta) = \begin{cases} 0 & \text{for } \theta \in [-\pi; -(\theta_b + \theta_{so})/2] \\ (N_c/\theta_{so})(\theta_b + (\theta_b + \theta_{so})/2) & \text{for } \theta \in [-(\theta_b + \theta_{so})/2; -(\theta_b - \theta_{so})/2] \\ N_c & \text{for } \theta \in [-(\theta_b - \theta_{so})/2; (\theta_b + \theta_{so})/2] \end{cases} \quad (20)$$

where θ_b is the coil opening and θ_{so} is the slot opening.

Afterward, the total flux linkage of one phase is obtained by adding the fluxes of all coils belonging to this phase. The coil configuration should be taken account in this stage. Afterward, the back EMFs under n_{sp} speed are calculated by

$$\begin{pmatrix} E_a \\ E_b \\ E_c \\ E_d \\ E_e \end{pmatrix} = n_{sp} \frac{d}{d \Delta} \begin{pmatrix} \Psi_a \\ \Psi_b \\ \Psi_c \\ \Psi_d \\ \Psi_e \end{pmatrix}. \quad (21)$$

The back EMF is shown in Fig. 9. The computation is done at rated speed 15 000 r/min. The results obtained from the proposed method are in agreement with the FEM ones.

The RMS value of proposed method is 191.93 V, which is slight higher than that obtained from 3-D FEM model 185.55 V. This is mainly caused by the end effect, which means the amplitude of magnetic flux density is dropped at the inner and outer radii.

According to the Maxwell tensor equation, the torque can be computed by

$$T = \frac{LR_a^2}{\mu_0} \int_0^{2\pi} B_r(R_a, \theta) \cdot B_t(R_a, \theta) d\theta \quad (22)$$

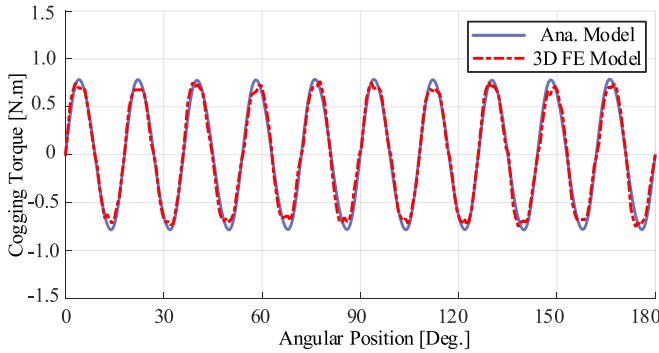


Fig. 10. Comparison of cogging torque.

where L is axial length, and R_a is the average radius of air gap.

Fig. 10 shows the cogging torque of prototype. As shown in Fig. 10, the proposed method is able to predict the cogging torque waveform with high degree of accuracy. The amplitude is also slight higher than FEM model.

B. Partial Demagnetization Permeance

It should be noted that the demagnetization of single PM may be asymmetric in the actual operation. In this condition, the single PM can be divided into several pieces, and hence, the flux density of each piece can be calculated by area-average magnetization factor, afterward, and approximate flux density of single PM can be obtained by superposition principle. Moreover, the demagnetization is affected by temperature, loss, operating condition, etc. in real operation; therefore, it is necessary to collaborate with other models to consider them properly. In this paper, we focus on the demagnetization model which is the core of analysis procedure.

In order to verify the analytical model, a representative and simple demagnetization condition is presented, viz., the PMs are assumed to have uniform partial/whole demagnetization damage. The space distribution of permanent magnets is shown in Fig. 11. The magnetization factor K_a has a value between 0 and 1. Here, 0 represents full demagnetization and 1 represents a healthy magnet. The permanent magnets with magnetization direction 90° (3# and 7#) are selected to investigate partial demagnetization since the influence is much higher than other PMs. The remanence of the whole 3# PM is demagnetized to 75%. With regards to the 7# PM, 50% of the PM is demagnetized to 75% while the other part is healthy, which is partial demagnetization. The rest PMs are healthy.

Fig. 12 shows the radial and tangential air-gap flux density components contributed by the demagnetized permanent magnets. It can be seen that the results agree well with that of FE model at the demagnetized area while error occurs at other area. However, it will be vanished once superposition is applied.

After superposition applied, the magnetic flux distribution contributed by all magnets is shown in Fig. 13. It can be seen that the amplitude of flux density is decreased comparing with the healthy machine and the results match well with FE results.

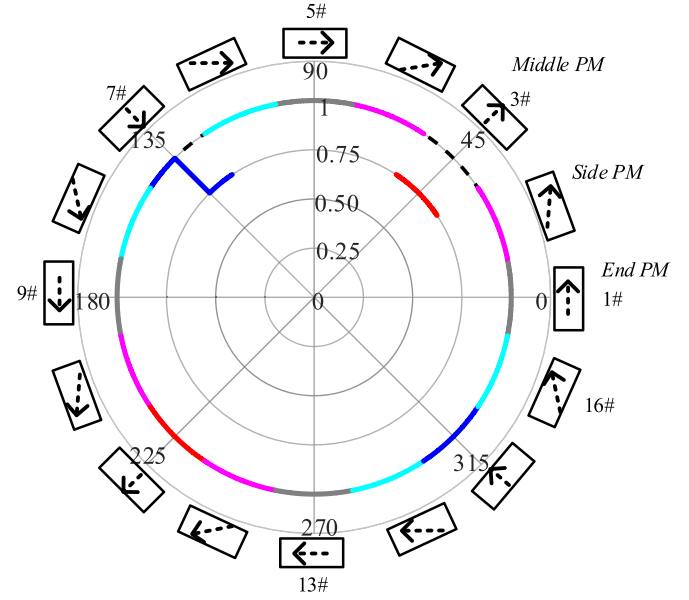


Fig. 11. Space distribution of PM remanence.

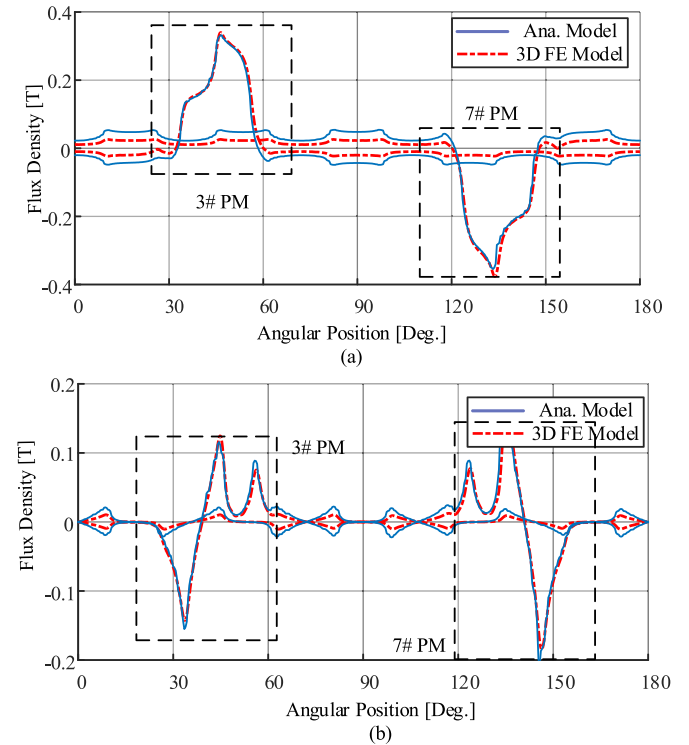


Fig. 12. Airgap flux density waveforms of demagnetization permanent magnets and FEM. (a) Radial component. (b) Tangential component.

Fig. 14 shows the back EMF waveforms calculated by the proposed method and the FEM model. It is shown that the results of the proposed method agree well with the FE model.

Fig. 15 shows the FFT analyze of the back EMF of healthy condition and partial demagnetization condition obtained from the proposed model. It is shown that the harmonics change significantly under partial demagnetization.

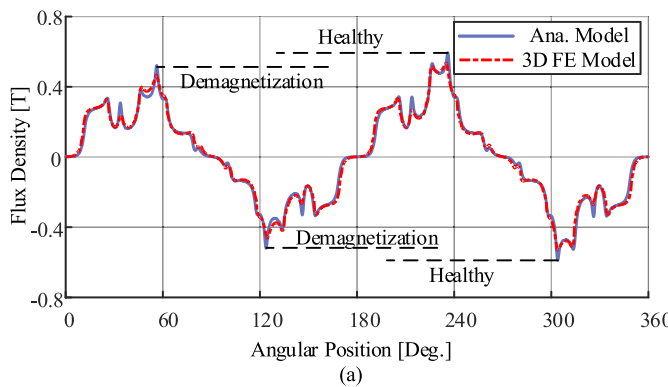


Fig. 13. Total airgap flux density waveforms under partial demagnetization. (a) Radial component. (b) Tangential component.

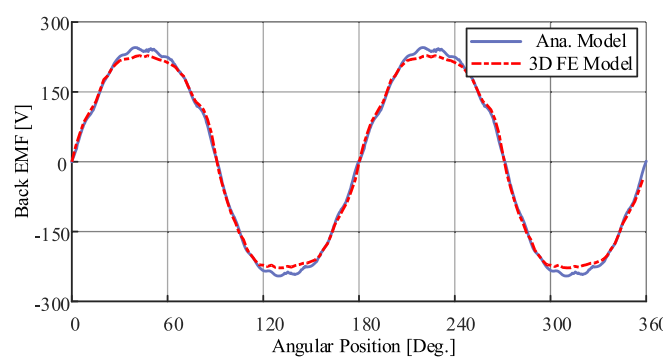


Fig. 14. Back-EMF under partial demagnetization condition.

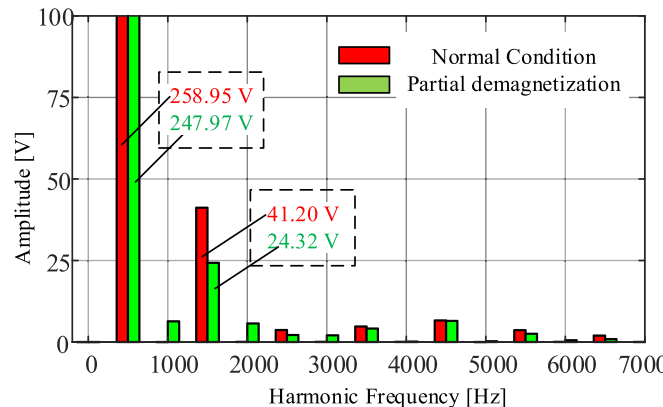


Fig. 15. FFT of back EMF.

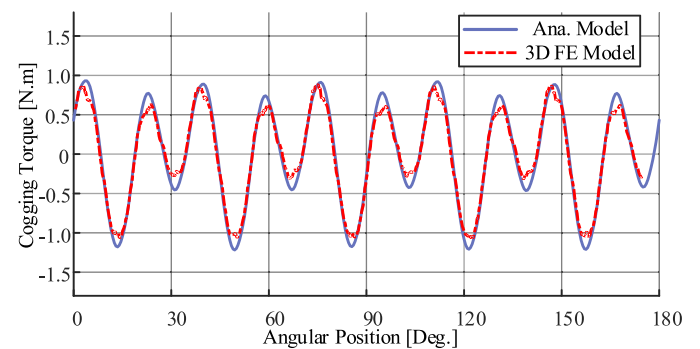


Fig. 16. Comparison of cogging torque under partial demagnetization.

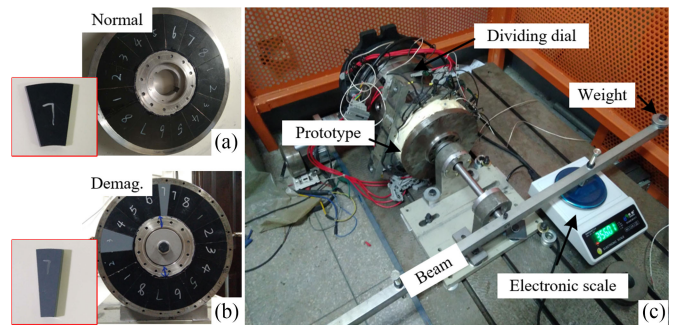


Fig. 17. Prototype machine and the experimental set-up. (a) Normal. (b) Demagnetization. (c) Cogging torque test.

The cogging torque waveform of the partial demagnetization is calculated by the analytical and FE methods and shown in Fig. 16. As shown, the proposed method with the SD model has high accuracy for predicting the cogging torque with partial demagnetization. Moreover, the cogging torque obtained from the proposed model is slight higher than that of FE model because of the neglecting of end effect. The waveform of cogging torque shown in Fig. 16 has a short period and is asymmetrical compared to the healthy motor.

C. Computation Time

In terms of the computation time, the 3-D FEM requires 4 (days) 6 (h) to obtain the basic performance when the model has 1507845 elements (i7-4800 MQ @ 2.70(GHz) CPU, 32 (GB) RAM). If multislice 2-D FE model is adopted, it still costs about 22 min to obtain the results. The hybrid method proposed in this paper, on the other hand, requires only a few seconds to get the final results. Therefore, the model is much faster than FEM.

VI. EXPERIMENTAL VALIDATION

To validate the proposed approach, PMs with low remanence are used to create the demagnetization condition. Fig. 17(a) and (b) shows the rotor with normal and demagnetization condition, respectively. It should be noticed that the gray PMs in Fig. 17(b) are the magnets with low remanence, and the AFPM presents a separable component that is simple in structure and convenient for testing and measuring. The test rig for cogging torque is

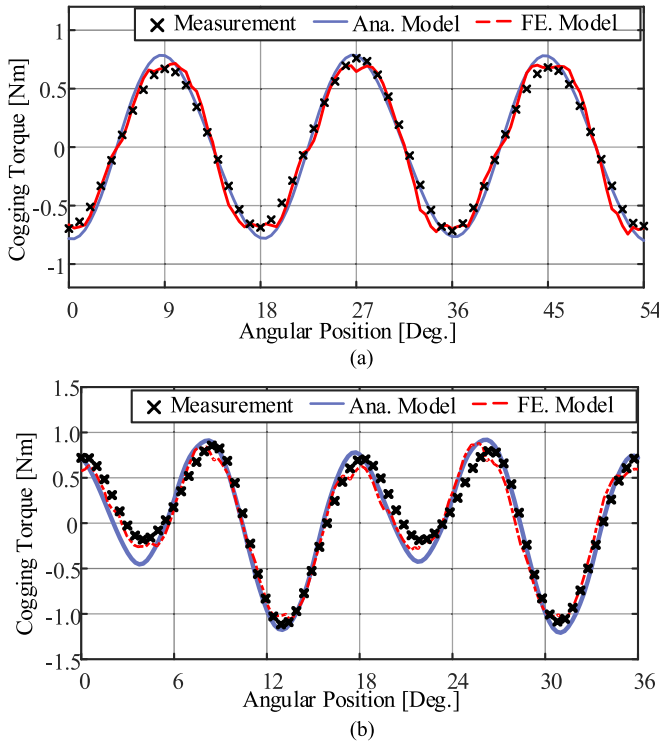


Fig. 18. Comparison of cogging torque between measurement, proposed and FE model. (a) Normal. (b) Demagnetization.

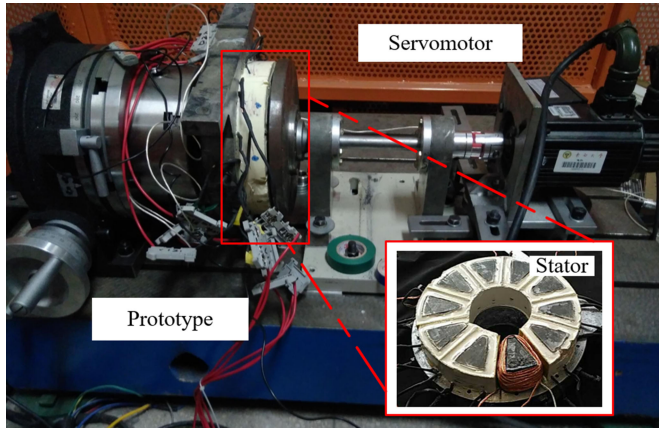


Fig. 19. Back EMFs experimental setup.

shown in Fig. 17(c). The prototype is clamped by a dividing dial and a beam is fixed to the rotor shaft. A weight is fixed on one side of beam in order to keep the force acts on the scale at any rotor position, moreover, the weight can reduce the influence of friction.

The cogging torque waveform can be obtained by the lever principle from the read of the electronic scale. Fig. 18(a) and (b) shows the comparison between the proposed approach, FE model predicted and measured cogging torque waveforms under normal and demagnetization conditions, respectively. It can be found that an acceptable agreement has been achieved.

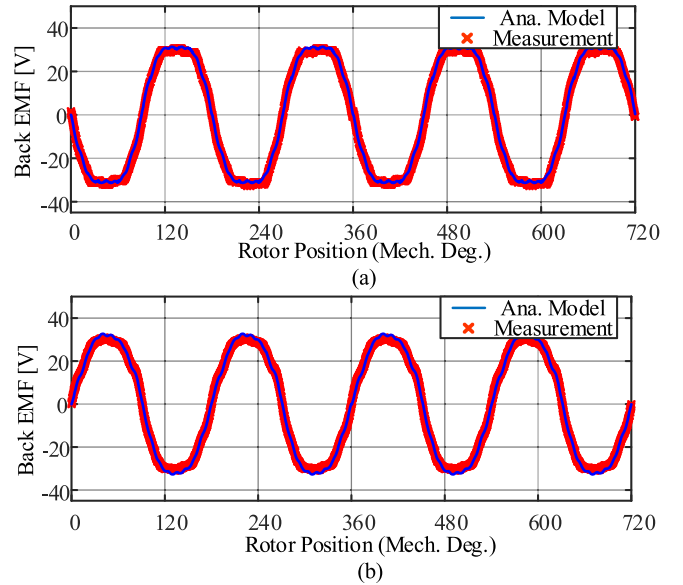


Fig. 20. EMFs results. (a) Normal. (b) Partial demagnetization.

The experimental setup for back EMFs and devices are shown in Fig. 19. In the test bench, the prototype is coupled with a servomotor via a coupling. Therefore, the AFPM machine can be driven by the servomotor.

A no-load test was done at 2000 r/min. The comparison between the analytical results and the experimental results is shown in Fig. 20. It can be seen that the results match well.

VII. CONCLUSION

This paper has presented an analytical method for calculating partial demagnetization in an AFPM machine with Halbach arrays. The AFPM machine was first transformed to a polar coordinate, which makes the model much more adaptive to either radial or axial flux machines. Then, the magnetization of PMs was equivalent to that produced by pairs of current sheets in order to model the partial demagnetization of single PM. Afterward, the magnetic field was predicted by the SD model and the superposition principle. The back EMFs and cogging torque were calculated according to the Maxwell's equations and a good agreement was achieved comparing to both FE model and experimental data with healthy and partial demagnetization PMs. The developed model can be used for analyzing the demagnetization in both AFPM and RFPM machines, with or without Halbach arrays.

REFERENCES

- [1] G. Oosthuizen, "Design of an ironless double-rotor radial flux air-cored permanent magnet machine," Stellenbosch University, South Africa, 2016.
- [2] O. Maloberti *et al.*, "3-D - 2-D dynamic magnetic modeling of an axial flux permanent magnet motor with soft magnetic composites for hybrid electric vehicles," *IEEE Trans. Magn.*, vol. 50, no. 6, pp. 1–11, Jun. 2014.
- [3] A. Hemeida, M. Taha, A. A. E. Abdallah, H. Vansompel, L. Dupré, and P. Sergeant, "Applicability of fractional slot axial flux permanent magnet synchronous machines in the field weakening region," *IEEE Trans. Energy Convers.*, vol. 32, no. 1, pp. 111–121, Mar. 2017.

- [4] F. Sahin, "Design and development of a high-speed axial-flux permanent-magnet machine," *Dep. Elect. Eng., Technische Univ. Eindhoven*, Eindhoven, The Netherlands, 2001.
- [5] T. D. Nguyen, K.-J. Tseng, S. Zhang, and T. D. Nguyen, "A novel axial flux permanent-magnet machine for flywheel energy storage system: Design and analysis," *IEEE Trans. Ind. Electron.*, vol. 58, no. 9, pp. 3784–3794, Sep. 2011.
- [6] P. J. Tavner, "Review of condition monitoring of rotating electrical machines," *IET Electr. Power Appl.*, vol. 2, no. 4, pp. 215–247, Jul. 2008.
- [7] A. Di Gerlando, G. M. Foglia, M. F. Iacchetti, and R. Perini, "Effects of manufacturing imperfections in concentrated coil axial flux PM machines: Evaluation and tests," *IEEE Trans. Ind. Electron.*, vol. 61, no. 9, pp. 5012–5024, Sep. 2014.
- [8] S. Zhu, M. Cheng, W. Hua, X. Cai, and M. Tong, "Finite element analysis of flux-switching PM machine considering oversaturation and irreversible demagnetization," *IEEE Trans. Magn.*, vol. 51, no. 11, pp. 1–4, Nov. 2015.
- [9] G. Choi, "Investigation of fault modes in permanent magnet synchronous machines for traction applications," Ph.D. dissertation, Dept. Elect. Comput. Eng., Univ. Wisconsin, Madison, WI, USA, 2016.
- [10] D. Torregrossa, A. Khoobroo, and B. Fahimi, "Prediction of acoustic noise and torque pulsation in PM synchronous machines with static eccentricity and partial demagnetization using field reconstruction method," *IEEE Trans. Ind. Electron.*, vol. 59, no. 2, pp. 934–944, Feb. 2012.
- [11] D. Lim, K. Yi, S. Jung, H. Jung, and J. Ro, "Optimal design of an interior permanent magnet synchronous motor by using a new surrogate-assisted multi-objective optimization," *IEEE Trans. Magn.*, vol. 51, no. 11, pp. 1–4, Nov. 2015.
- [12] P. Naderi, "Cage-rotor induction motor inter-turn short circuit fault detection with and without saturation effect by MEC model," *ISA Trans.*, vol. 64, pp. 216–230, 2016.
- [13] D. S. Mihić, M. V. Terzic, and S. N. Vukosavic, "A new nonlinear analytical model of the SRM with included multiphase coupling," *IEEE Trans. Energy Convers.*, vol. 332, no. 4, pp. 1322–1334, Dec. 2017.
- [14] Z. Q. Zhu, L. J. Wu, and Z. P. Xia, "An accurate subdomain model for magnetic field computation in slotted surface-mounted permanent-magnet machines," *IEEE Trans. Magn.*, vol. 46, no. 4, pp. 1100–1115, Apr. 2010.
- [15] L. J. Wu, Z. Q. Zhu, D. Staton, M. Popescu, and D. Hawkins, "Analytical prediction of electromagnetic performance of surface-mounted PM machines based on subdomain model accounting for tooth-tips," *IET Electr. Power Appl.*, vol. 5, no. 7, pp. 597–609, Aug. 2011.
- [16] Y. Zhou, H. Li, G. Meng, S. Zhou, and Q. Cao, "Analytical calculation of magnetic field and cogging torque in surface-mounted permanent magnet machines accounting for any eccentric rotor shape," *IEEE Trans. Ind. Electron.*, vol. 62, no. 6, pp. 3438–3447, Jun. 2015.
- [17] J. D. Bisschop, P. Sergeant, A. Hemeida, H. Vansompel, and L. Dupré, "Analytical model for combined study of magnet demagnetization and eccentricity defects in axial flux permanent magnet synchronous machines," *IEEE Trans. Magn.*, vol. 53, no. 9, pp. 1–12, Sep. 2017.
- [18] J. D. Bisschop, H. Vansompel, P. Sergeant, and L. Dupré, "Demagnetization fault detection in axial flux pm machines by using sensing coils and an analytical model," *IEEE Trans. Magn.*, vol. 53, no. 6, pp. 1–4, Jun. 2017.
- [19] N. Ertugrul, R. Hasegawa, W. L. Soong, J. Gayler, S. Kloeden, and S. Kahourzade, "A novel tapered rotating electrical machine topology utilizing cut amorphous magnetic material," *IEEE Trans. Magn.*, vol. 51, no. 7, pp. 1–6, Jul. 2015.
- [20] H. Hu, J. Zhao, X. Liu, and Y. Guo, "Magnetic field and force calculation in linear permanent-magnet synchronous machines accounting for longitudinal end effect," *IEEE Trans. Ind. Electron.*, vol. 63, no. 12, pp. 7632–7643, Dec. 2016.
- [21] A. Hemeida and P. Sergeant, "Analytical modeling of surface PMSM using a combined solution of Maxwell's equations and magnetic equivalent circuit," *IEEE Trans. Magn.*, vol. 50, no. 12, pp. 1–13, Dec. 2014.
- [22] Z. Q. Zhu, D. Howe, and C. C. Chan, "Improved analytical model for predicting the magnetic field distribution in brushless permanent-magnet machines," *IEEE Trans. Magn.*, vol. 38, no. 1, pp. 229–238, Jan. 2002.
- [23] G. Houdouin, G. Barakat, B. Dakyo, and E. Destobbeleer, "A winding function theory based global method for the simulation of faulty induction machines," in *Proc. IEEE Int. Electr. Mach. Drives Conf.*, 2003, vol. 1, pp. 297–303.



Baocheng Guo (S'14–M'18) received the B.E. degree in electrical engineering from China University of Petroleum, Qingdao, China, in 2009, the M.E. degree in electrical engineering from Harbin University of Science and Technology, Harbin, China, in 2014, and the Ph.D. degree in electrical engineering from Southeast University, Nanjing, China, in 2017.

He is currently a Postdoctoral Researcher at Southeast University, Nanjing, China. His main interests are the electromagnetic field computation, and development of fast multiphysics models of electrical machines.



Yunkai Huang received the M.Sc. and Ph.D. degrees in electrical engineering from the Southeast University, Nanjing, China, in 2001 and 2007, respectively.

He is currently a Professor with the School of Electrical Engineering, Southeast University. His research interests include design and control of PM machine and high speed machine, applications in domestic appliances, electric vehicles, railway traction, all-electric ships, more-electric aircraft, and wind power generation systems.



Fei Peng (S'15–M'16) received the B.S. and M.S. in electrical engineering from Southeast University, Nanjing, China, in 2010 and 2012, respectively, and the Ph.D. degree in electrical and computer engineering from McMaster University, Hamilton, ON, Canada, in 2016.

After that he worked as a Postdoctoral Fellow at the McMaster Institute for Automotive Research and Technology (MacAuto), McMaster University. In December 2016, he joined the School of Electrical Engineering at Southeast University, Nanjing, Jiangsu, China, as an Assistant Professor. His research interests include optimal design and control of power converters, modeling, and digital control of motor drives.



Jianning Dong (S'10–M'17) received the B.S. and Ph.D. degrees in electrical engineering from Southeast University, Nanjing, China, in 2010 and 2015, respectively.

He is an Assistant Professor at the Delft University of Technology since 2016. Before joining TU Delft, he was a Postdoctoral Researcher at McMaster Automotive Resource Centre (MARC), McMaster University, Hamilton, ON, Canada. His main research interests include design, modeling, and control of electromechanical systems.